



Research on the Mechanical Properties of Single-Lap Rivet-Bonded Hybrid Joint Considering the Rivet Forming Process

X. Han¹ · L. Z. Ren¹ · X. Xu² · L. Ying³ · C. W. Wu¹ · W. B. Hou^{3,4}

Received: 10 January 2024 / Accepted: 17 June 2024 / Published online: 26 June 2024
© Society for Experimental Mechanics 2024

Abstract

Background This paper investigates the mechanical properties and failure behaviours of rivet-bonded hybrid joints composed of aluminium adherends and steel rivets under quasi-static tensile loading.

Objective The damage law of hybrid joints is studied to provide a reference for the design and manufacture of hybrid joints.

Methods Tensile tests were conducted on aluminium and steel specimens at various triaxial stress levels. The corresponding finite element model (FEM) was developed to verify the Johnson–Cook damage parameters of the studied metals. The hybrid joint considering the rivet forming process was constructed through FE modelling using the Johnson–Cook failure criterion and Cohesive Zone Model (CZM), which was then validated with the experimental results.

Results Experimental results of the hybrid joint showed that a typical two-stage failure: 1) the adhesive layer bears the majority of the load during the initial loading stage, and 2) the adhesive layer completely fails after reaching the peak load and the rivet solely bears the load subsequently.

Conclusions The riveting process did not cause damage to the adhesive layer, which ensured the reliability of the manufacturing techniques of the hybrid joint. And the yielding of rivets may buffer the immediate failure of hybrid joints.

Keywords Hybrid joint · Tensile properties · Failure behaviour · Damage mechanics · Numerical analysis

Introduction

Mechanical fastening and adhesive bonding are the main connecting methods in fields such as aerospace, ocean, and automotive transportation [1–3]. By utilizing the physical or chemical reaction between the adhesive and the base material to connect the substrate, the bonded joint provides a more uniform stress distribution, effectively avoids stress concentration, improves the vibration resistance, and reduces

structural weight. It is widely used in the manufacturing process of structural components such as aircraft bodies, fuel tanks, and doors in the aviation industry. However, the bonded joint cannot be disassembled without damage, and there are issues such as poor aging and impact resistance, sensitivity to environmental factors such as humidity and temperature, etc. [4–8]. Hybrid joints based on adhesive bonding and mechanical fastening combine the advantages of the above two to ensure greater load-bearing capacity, stronger fatigue resistance, environmental adaptability, and energy absorption characteristics [9, 10].

The load transfer path, load distribution, and failure mode of hybrid joints are extremely complex. There are still challenges to understanding the failure mechanism, improving stiffness matching between bonded joints and mechanical fastened joints using rivets or bolts, and enhancing the load distribution balance of hybrid joints. EI Zaroug et al. [11] found in their investigation of hybrid joints by bolts that the adhesive layer always reached complete damage before the bolt or substrate. The energy absorbed by hybrid joints was almost equal to the total energy of bonded joint and bolted joint. The mechanical properties of hybrid joints were

✉ W. B. Hou
houwb@dlut.edu.cn

¹ School of Mechanics and Aerospace Engineering, Dalian University of Technology, Dalian, China

² Automotive Engineering Research Institute, BYD Auto Industry Co, Ltd, Shenzhen, China

³ State Key Laboratory of Structural Analysis, Optimization and CAE Software for Industrial Equipment, School of Mechanical Engineering, Dalian University of Technology, Dalian, China

⁴ Ningbo Institute of Dalian University of Technology, Ningbo, China

affected by process parameters such as the number of rivets, material, distribution position, adhesive layer thickness, and overlap length in the hybrid connection. Sadowski et al. [12] investigated the effect of geometric layout of three rivets on the strength of hybrid joints. The research found that the stress distribution in the overlap area of hybrid joints with a rivet layout of 1 + 2 was more uniform than in other situations. The tensile strength of the hybrid joint was about 3% higher than that of bonded joint, and the energy absorbed was 1.7 times higher than it. Kang et al. [13] studied the tensile load and fatigue life of adhesively bonded and hybrid CFRP–steel joints with different overlap lengths were analysed and compared. It has been found that adhesives with relatively high stiffness can lead to inappropriate load distribution, and hybrid joints exhibit lower tensile load capacity and fatigue life than bonded joints. Sousa et al. [14] analysed the fatigue performance and failure modes of hybrid joints with different overlap lengths. Wang et al. [15] examined the surface strain, out-of-plane displacement, and tensile displacement of the single-lap bolt joints to anticipate when the joints would fail, how they would expand, and how bolt fracture would ultimately fail. Zhang et al. [16] found that the polyurethane adhesive with a thickness of 0.5 mm had the highest strength when studying the hybrid joint composed of plain weave composite materials and 7075 aluminium alloy. There were three typical stages in the tensile failure process of hybrid joints: firstly, the adhesive layer and rivets shared the load; then the adhesive layer gradually broke; finally, the rivet bore the load alone. Kelly [17] concluded the influences of some design parameters on load transfer and found that the load transmitted by bolts increased with the increase of the thickness of adherend and adhesive. And it decreased as the overlap length, spacing, and bonding method increased.

Refined FEMs have been established to analyse the mechanical property and failure mechanism of hybrid joints. Chowdhury et al. [18] established a FEM of carbon fibre reinforced polymer for bolted, bonded, and hybrid joints. The nonlinear mechanical properties of adhesive were considered, while the theory of progressive damage and multi continuity was introduced. The results indicated that it was crucial to place fasteners closer to the overlap ends to suppress peel stress and delay early crack initiation. In order to understand the principle of load distribution and how to achieve maximum efficiency in load distribution, Bodjona et al. [19] conducted extensive global sensitivity analysis on the calculation model of single-lap hybrid joints, and determined that the yield strength of adhesive was the most important influencing factor. Edge distance ratio is referred to by the acronym E/D. The joint E/D ratio, adhesive hardening slope, and adhesive thickness were found to be other significant factors influencing load sharing. Raju et al. [20] established a FEM to study the hybrid joint using

interference-fit bolts instead of clearance-fit bolts. The results indicated that the joint bearing capacity of interference-fit joint was 10% higher than that of clearance-fit joint. The bolt would carry the load as soon as the interference-fit joint was loaded. Esmaeili-Goldarag et al. [21] investigated the clamping force variation of double lap pure bolts and hybrid joints under longitudinal tensile load. The results indicated that the longitudinal tensile load reduced the clamping force.

The previous works focused on design parameter, mechanical property and failure behaviour. Few of them considered the effect of the internal stress induced from the rivet forming process on the joint, as well as the damage in the substrate and adhesive layer [22–25]. In this paper, tensile properties of a single-lap rivet-bonded hybrid joint were investigated experimentally, and then a defined FEM containing Johnson–Cook failure criterion and CZM with consideration of the riveting process was established. The damage parameters of Johnson–Cook were obtained through testing of standard tensile specimens, notched specimens, and shear specimens. The failure behaviour of hybrid joints and stress distribution in the overlap zone were numerically studied.

Experimental Methods

Design of Hybrid Joint and Mechanical Properties Characterization

The schematic of the single-lap rivet-bonded hybrid joint is shown in Fig. 1, as in accordance with ASTM D5868 [26]. The adhesive material is Araldite 2015, which is a widely studied two-component epoxy adhesive. The selection of Araldite 2015 is primarily attributed to its superior bonding capacities, mechanical strength, and exceptional chemical resistance. Its outstanding bonding performance ensures the reliability and durability, which is crucial in the automotive, ocean and aerospace engineering. Furthermore, it is convenient for the FE modelling that Araldite 2015 has been thoroughly investigated by many researchers and the mechanical properties can be easily obtained. The adhesive mechanics property parameters are as shown in Table 1 [27, 28]. The rivet selected for the production of the hybrid joint is a blind hole rivet of BB-C-FIX0604 series produced by Fast-Fix Rivet Corporation, and the rivet material is 304 stainless steel. The adherend is 6061 aluminium plates. In the aerospace industry, the lightweight and corrosion-resistant properties of 6061 aluminium alloy make it an ideal choice for aircraft structures. Meanwhile, the strength and durability of 304 stainless steel rivets ensure secure joints in these critical applications. Similarly, in the automotive industry, both materials are often used in the manufacture of lightweight and durable vehicle components. In order to accurately characterize the mechanical properties

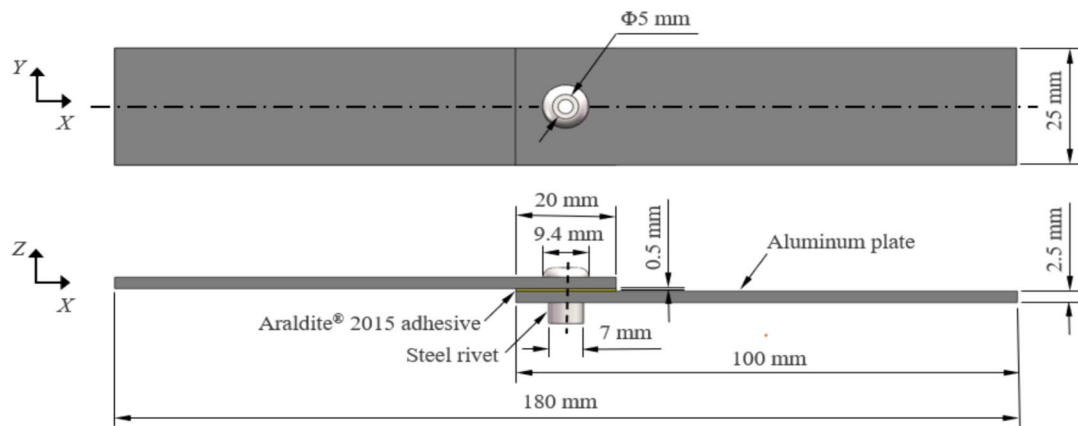


Fig. 1 Configuration and geometric parameters of the single-lap rivet-bonded hybrid joint

of 6061 aluminium alloy and 304 stainless steel, standard tensile specimens were prepared, as shown in Fig. 2(a). To determine the parameters of the Johnson–Cook failure criterion, it is necessary to obtain the corresponding failure strains of two metals under different stress states. Therefore, notched specimens and shear specimens were designed, as shown in Fig. 2(b) and (c). 304 stainless steel specimens were made of 3 mm thick plate, and 6061 aluminium alloy specimens were made of 2.5 mm thick plate. To ensure the accuracy of experiment, four samples were prepared for each group of experiments using wire cutting technology. During the testing process, the failure strain of the standard tensile specimen was obtained with an extensometer. The strain distribution of notched specimen and shear specimen was uneven, so the digital image correlation was used to measure their failure strain. The quasi-static tensile tests have been performed by using MTS universal testing machine, and a standard head displacement rate of 2 mm/min was conducted. The tensile experiments are shown in Fig. 3. Figure 4 shows the failure morphologies of specimens after fracture. The mechanical property parameters of 6061 aluminium alloy and 304 stainless steel obtained are shown in Table 2.

Table 1 Mechanical properties of Araldite 2015

Properties	Araldite 2015
Elastic modulus (GPa)	$E = 1.85$
Shear modulus (GPa)	$G = 0.56$
Tensile strength (MPa)	$f_n^0 = 21.63$
Shear strength (MPa)	$f_s^0 = f_t^0 = 17.9$
Poisson's ratio	$\nu = 0.33$
Fracture toughness (N/mm)	$G_n^C = 0.35, G_s^C = G_t^C = 2.8$
Curing temperature/time* (°C/min)	60/120

* manufacturer data

Manufacture of Hybrid Joint

The manufacturing process of single-lap rivet-bonded hybrid joints usually involves bonding, riveting, and curing, as shown in Fig. 5. First, the aluminium adherend was subjected to surface treatment, and the surface of the bonding area was sanded with 100-grit sandpaper. Then, impurities at the overlap interface were removed with acetone solution and allowed to dry naturally. The release agent was applied to the sides of the overlap area to ensure that only the bonding interface was bonded [29, 30]. The two-component epoxy adhesive of Araldite 2015 was fully stirred and evenly coated on the surface of the plate. Glass microspheres with a diameter of 0.5 mm were added to control the thickness of bonding layer

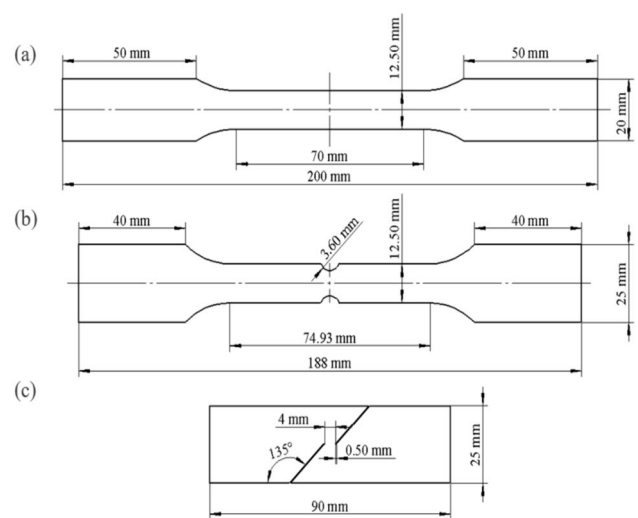


Fig. 2 Geometric details of (a) standard tensile specimen, (b) notched specimen, and (c) shear specimen

Fig. 3 Quasi-static tensile tests of (a) standard tensile specimen, (b) notched specimen, and (c) shear specimen

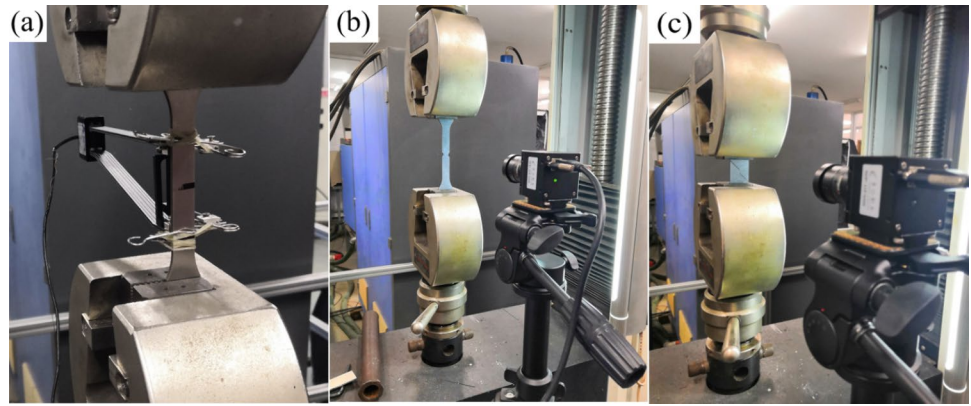


Fig. 4 Failure morphologies of (a) standard tensile specimen, (b) notched specimen, and (c) shear specimen

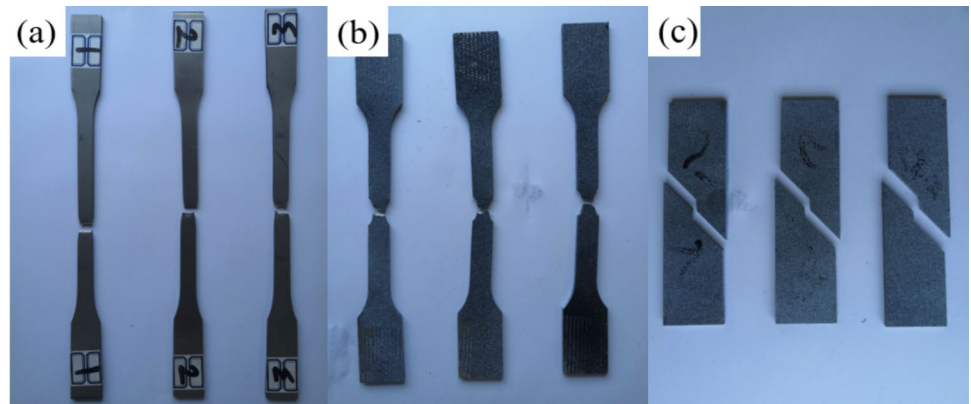


Table 2 Mechanical properties of 6061 aluminium alloy and 304 stainless steel

Properties	6061 aluminium alloy	304 stainless steel
Elastic modulus (GPa)	$E = 71.6 \pm 1.73$	$E = 196 \pm 2.11$
Poisson's ratio	$\nu = 0.33$	$\nu = 0.28$
Yield strength (MPa)	$\sigma_s = 252 \pm 3.56$	$\sigma_s = 248 \pm 2.77$
Ultimate strength (MPa)	$\sigma_b = 374 \pm 4.48$	$\sigma_b = 832 \pm 3.89$
Failure strain	Standard tensile specimen	0.26 ± 0.0163
	Notched specimen	0.33 ± 0.0141
	Shear specimen	0.20 ± 0.0082
		0.15 ± 0.0076

\pm refers to standard deviation

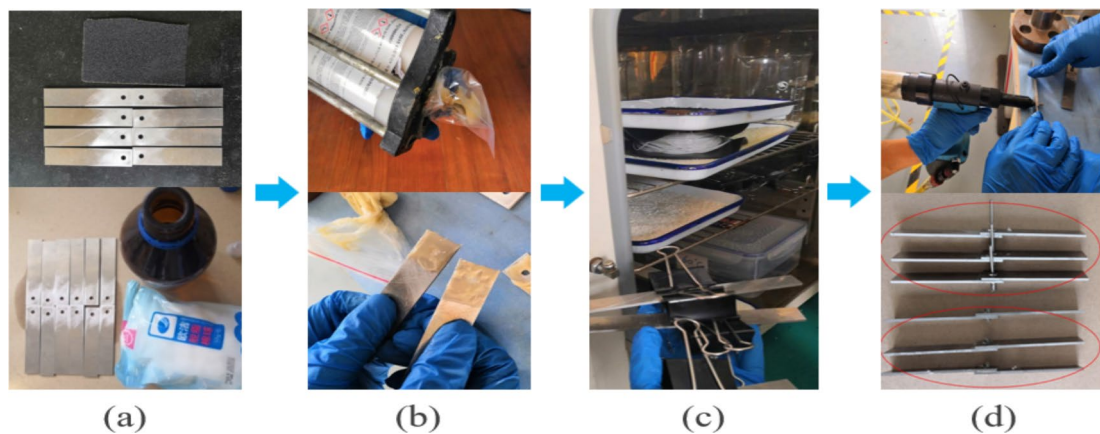


Fig. 5 Manufacturing process of single-lap rivet-bonded hybrid joints: (a) surface treatment, (b) adhesive coating, (c) adhesive curing, and (d) riveting

and the length of the bonding area of the specimen was controlled by wrapping high-temperature resistant tape [31, 32]. Araldite 2015 was cured at 60 °C for 4 h in an electric thermostatic drying oven. Finally, riveting was performed with a pneumatic riveting gun after the adhesive was completely cured.

Quasi-Static Tensile Test of Hybrid Joint

The quasi-static tensile test was carried out on the single-lap rivet-bonded hybrid joint by the universal testing machine. The clamping depth of the fixture was set at 30 mm, and the tensile load was applied at a constant rate of 2 mm/min until the specimen completely failed, as shown in Fig. 6. The loading rate of 2 mm/min selected in this study is considered appropriate to ensure consistency with previous studies and facilitate quasi-static deformation of the specimen, and further minimizing the potential for abrupt collapse or uneven stress distribution. At the same time, a high-speed camera was used to record the failure process. The hybrid joint was tested with 4 replicates to record the corresponding mean value and standard deviation.



Fig. 6 Quasi-static tensile loading of the single-lap rivet-bonded hybrid joint

Force–Displacement Curve of Hybrid Joint

The experimental force–displacement curve of the single-lap rivet-bonded hybrid joint is shown in Fig. 7. The failure process of the hybrid joint can be divided into two stages. At the small-displacement stage, the hybrid joint gradually begins to bear load with the increase of displacement. The force–displacement relationship of the hybrid joint is approximately linear, indicating that the joint is in the elastic deformation stage, and its stiffness does not change greatly. When the displacement exceeds 0.6 mm, the load reaches the upper limit of the hybrid joint, and then the force drops sharply with the rapid fracture of the adhesive layer, which is accompanied by the crisp fracture sound caused by the cohesive failure. The rivet limits the release of elastic potential energy of the hybrid joint. In contrast, when a bonded joint reaches peak load, the carrying capacity quickly disappears, so a sudden rupture may result in a serious structural safety accident [11, 16]. With the increase of displacement, the hybrid joint comes to the large-displacement stage. At this time, as the only rivet with bearing capacity, it undergoes plastic collapse and is in the yield stage. The bearing capacity of the joint increases slowly. When the displacement reaches 5 mm, the hybrid joint reaches the bearing limit of the rivet, which slips away from the riveting hole. Finally, the hybrid joint completely fails.

Modelling Details

Constitutive Behaviour of Material Damage

It is necessary to incorporate different damage criteria to different materials in the FE modelling stage. Johnson–Cook failure criterion is commonly used to simulate the

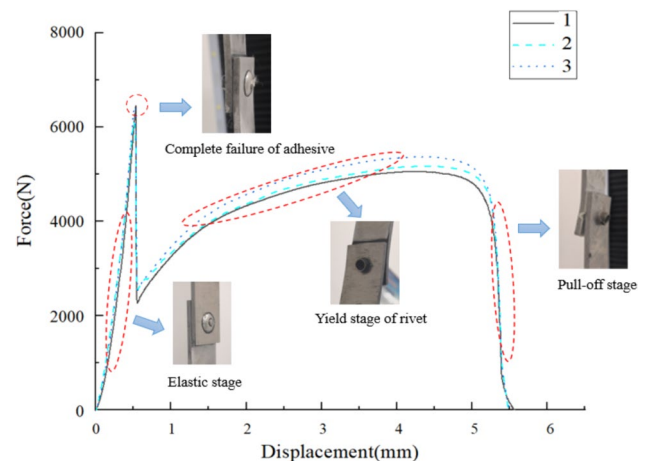


Fig. 7 Force–displacement curve of the single-lap rivet-bonded hybrid joint

mechanical behaviour and failure process of metals under large deformation, high strain rate and various temperature environments [33, 34]. Cohesive Zone Model (CZM) is widely used to simulate the damage evolution in the adhesive layer [35–38]. The CZM of Araldite 2015 has been studied by various researchers. After examining DCB aluminium alloy specimens with an adhesive layer thickness of 3 mm, Campilho RDSG et al. determined that the trapezoidal CZM is suitable for defining these specimens [39]. Meanwhile, Sadeghi MZ et al. found that the bi-linear CZM is adequate for single-lap joints with thinner adhesive thickness [40]. In this study, based on the available literatures, the bi-linear CZM was adopted for characterizing the adhesive layer.

Johnson–Cook Failure Criteria

The yield stress is determined by strain, strain rate and temperature in the Johnson–Cook failure criterion. Johnson–Cook hardening model is used to simulate the mechanical behaviour of materials in the plastic deformation stage. Its constitutive relationships are as follows:

$$\sigma^0 = \left[A + B \left(\bar{\epsilon}^{pl} \right)^n \right] (1 - \hat{\theta}^m) \quad (1)$$

where σ^0 and $\bar{\epsilon}^{pl}$ are the yield stress and the equivalent plastic strain, respectively. A , B , n and m are the material parameters, and $\hat{\theta}$ is the dimensionless temperature parameter. The Johnson–Cook hardening parameters of 6061 aluminium alloy and 304 stainless steel are obtained by fitting the least square method, as shown in Table 3. Similar to Johnson–Cook hardening model, the failure strain of materials is affected by stress state, strain rate and temperature. Johnson–Cook failure model is based on the cumulative damage criterion. Damage variable ω is defined as:

$$\omega = \sum \left(\frac{\Delta \bar{\epsilon}^{pl}}{\bar{\epsilon}_f^{pl}} \right) = \begin{cases} \geq 1 & \text{damage} \\ < 1 & \text{undamage} \end{cases} \quad (2)$$

Table 3 Damage parameters of Johnson–Cook

Parameters	304 stainless steel	6061 aluminium alloy
A	320	257.5837
B	1733	419.7005
n	0.8621	0.6678
d_1	1.47	0.777
d_2	-1.32	-0.577
d_3	1.0813	0.3294

where $\Delta \bar{\epsilon}^{pl}$ is the equivalent plastic strain increment. $\bar{\epsilon}_f^{pl}$ is the failure strain, which is defined as:

$$\bar{\epsilon}_f^{pl} = \left[d_1 + d_2 \exp \left(d_3 \frac{p}{q} \right) \right] \left[1 + d_4 \ln \left(\frac{\dot{\bar{\epsilon}}^{pl}}{\dot{\epsilon}_0} \right) \right] (1 + d_5 \hat{\theta}) \quad (3)$$

where d_1 , d_2 and d_3 are obtained by fitting the stress triaxiality to the corresponding failure strain. d_4 is the strain rate sensitivity coefficient. d_5 is the temperature sensitivity coefficient. $\dot{\bar{\epsilon}}^{pl}$ is the equivalent plastic strain rate. $\dot{\epsilon}_0$ is the reference strain rate. Without considering temperature and strain rate, the above equation can be simplified as:

$$\bar{\epsilon}_f^{pl} = d_1 + d_2 \exp \left(d_3 \frac{p}{q} \right) \quad (4)$$

For the calculation of stress triaxiality of notched specimens, the following simplified formula is introduced:

$$\frac{p}{q} = \frac{1}{3} + \ln \left(1 + \frac{a}{2R} \right) \quad (5)$$

where a and R are half of the minimum section size and notched arc radius of specimens, respectively. The stress triaxialities of standard tensile specimen, notched specimen, and shear specimen are 0.333, 0.775, and 0, respectively.

Cohesive Zone Modelling of the Adhesive Layer

The CZM suggests that the traction of the adhesive layer increases with the separation of crack tip, until the traction reaches the initial moment of material damage. The traction decreases with the separation of crack tip during the damage evolution stage until the material completely fails. As shown in Fig. 8, a bilinear interface law was adopted by built-in material model in ABAQUS/Explicit.

In the linear elastic stage, the relationship between traction t and separation δ satisfies the following:

$$t_i = K_i \delta_i, \quad i = n, s, t \quad (6)$$

where n , s and t represent the normal direction and two shear directions. Damage criteria of cohesive layer is shown below:

$$\left(\frac{\langle t_n \rangle}{t_n^0} \right)^2 + \left(\frac{t_s}{t_s^0} \right)^2 + \left(\frac{t_t}{t_t^0} \right)^2 = \begin{cases} \geq 1 & \text{damage} \\ < 1 & \text{undamage} \end{cases} \quad (7)$$

where t_n^0 , t_s^0 and t_t^0 represent the maximum traction corresponding to the normal direction and the two shear directions, respectively.

The damage evolution law describes the rate at which the material stiffness is degraded once the corresponding initiation criterion is reached. A scalar damage variable D

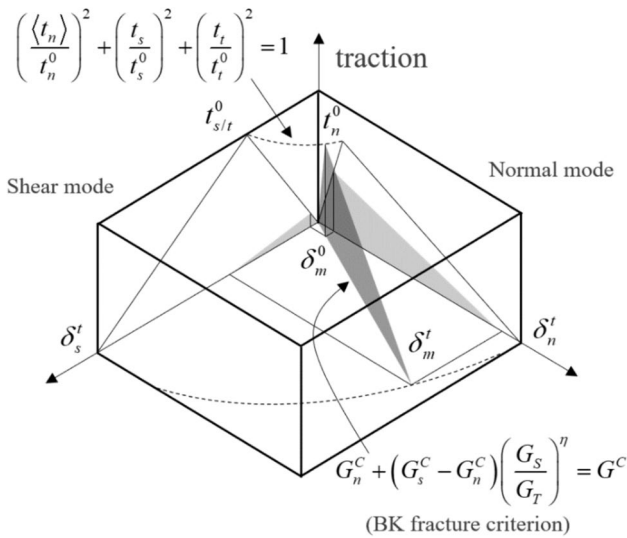


Fig. 8 Traction–separation law of Cohesive Zone Model

represents the overall damage in the material and captures the combined effects of all the active mechanisms. The stress components of the traction–separation model are affected by the damage according to:

$$t_i = (1 - D)\bar{t}_i, \quad i = n, s, t \tag{8}$$

where $\bar{t}_i (i = n, s, t)$ are the stress components predicted by the elastic traction–separation behaviour for the current strains without damage. In this study, the damage evolution depends on the total fracture energy which is based on BK energy criterion is described as follows:

$$G_n^C + (G_s^C - G_n^C) \left(\frac{G_s}{G_T} \right)^\eta = G^C \tag{9}$$

where G_n^C and G_s^C are the critical fracture energies, and η is exponential constant.

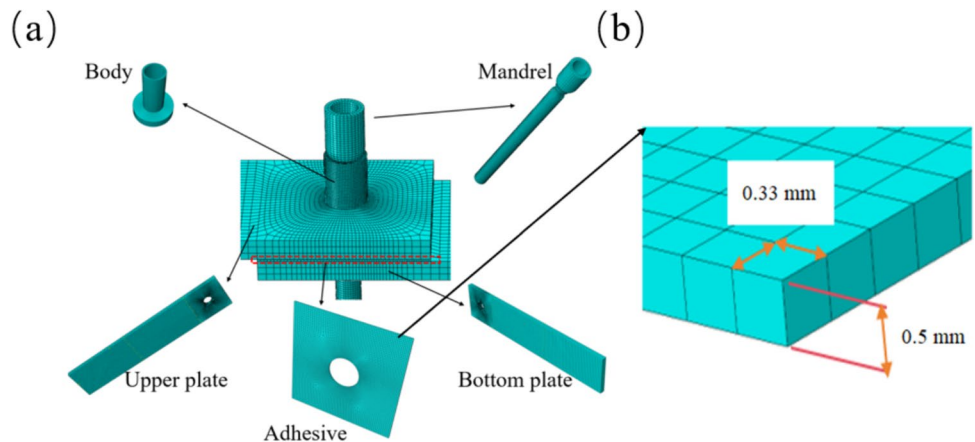
FEM of Rivet-Bonded Hybrid Joint Subject to Tensile Loading

The quasi-static tensile loading of the single-lap rivet-bonded hybrid joint was simulated by ABAQUS/Explicit. A typical hybrid joint model is shown in Fig. 9, which is composed of five parts: upper plate (C3D8R: 8-node linear brick), bottom plate (C3D8R: 8-node linear brick), adhesive layer (COH3D8: 8-node three-dimensional cohesive element), rivet body (C3D8R: 8-node linear brick) and mandrel (C3D8R: 8-node linear brick). Due to the high strain gradients existed around the plate hole, a refined mesh was adopted. The element size of the upper plate and the bottom plate is 0.8 mm. The element size of adhesive layer is 0.33 mm. In order to accurately simulate the deformation details, the rivet body was divided into 6238 elements with a size of 0.15 mm. There are contact relationships between the mandrel, the rivet body and the plate. Surface-to-surface contact was employed for the above contact pairs.

A mesh size convergence study was further conducted, to compare the changes in the force–displacement curves of the riveted hybrid joint under tensile loading. As can be seen in Fig. 10, the mesh size of the adhesive area was set to 0.33 mm, and this region was further refined to 0.10 mm. The peak load as well as failure displacement generally converge to a certain value, with a minor relative difference of 1.01% between the peak loads.

In this research, the deformation of the rivet body and plates caused by the mandrel in the riveting forming process was considered. The FEM was modelled as two analysis steps: the riveting forming process step and quasi-static tension step. In the first step, fixed constraints in three coordinate directions were imposed on the lower surface of a rivet body, and the displacement loading was applied in the z direction. The upper and lower surfaces of plates were subjected to displacement constraints in the x and y directions, as shown in Fig. 11(a). In the second step,

Fig. 9 FEM of (a) the single-lap rivet-bonded hybrid joint and (b) mesh size of the adhesive layer



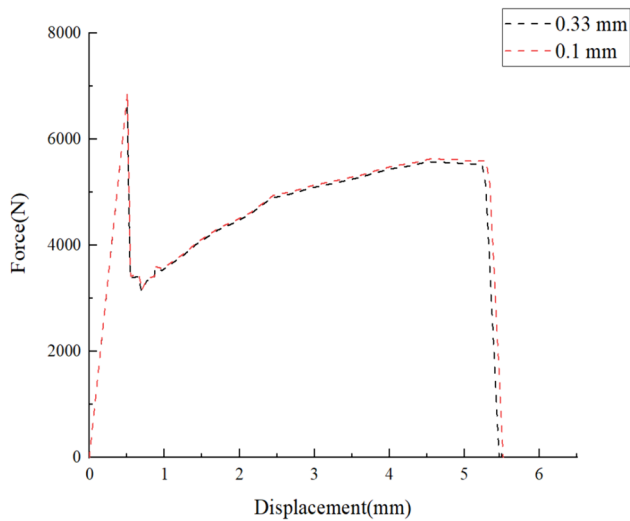


Fig. 10 Force–displacement curves of the riveted hybrid joints with different mesh sizes of the adhesive layer

the upper plate was fixed, and the lower plate was subjected to displacement loading in the x direction. Rivet rotation was restricted in the x and z directions, as shown in Fig. 11(b). The speed of displacement loading was

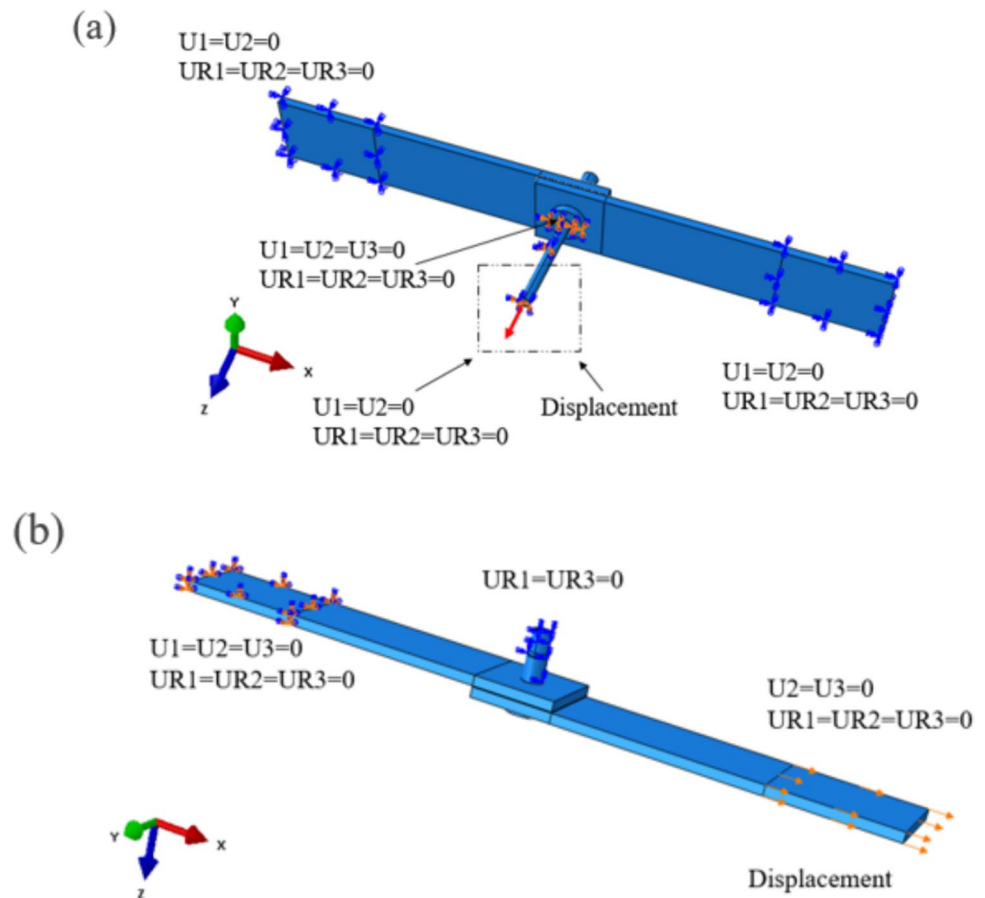
gradually increased from 0 to 2 mm/min, in order to avoid excessive momentum resulting in distortion of the numerical model.

Results and Discussion

Validation of Johnson–Cook Failure Model

The premise of accurate prediction is the precise definition of material parameters in FEM. Therefore, it is essential to verify the Johnson–Cook damage parameters in Table 3 by simulations. The force–displacement behaviour comparison between the experiment and simulation is shown in Fig. 12. The error between the standard tensile specimen, the notched specimen and the simulated peak load is within 10%. It is worth noting that there is an assembly gap between the loading fixture and the universal testing machine, which will lead to differences between the experimental curve of the initial elastic part and the finite element simulation curve. The peak load of the shear specimen is consistent with that of the simulation. Due to the small deformation of the shear specimen, the failure displacement of the simulation specimen is different from that of the experiment. In terms of

Fig. 11 Boundary conditions of (a) riveting forming process and (b) quasi-static tension



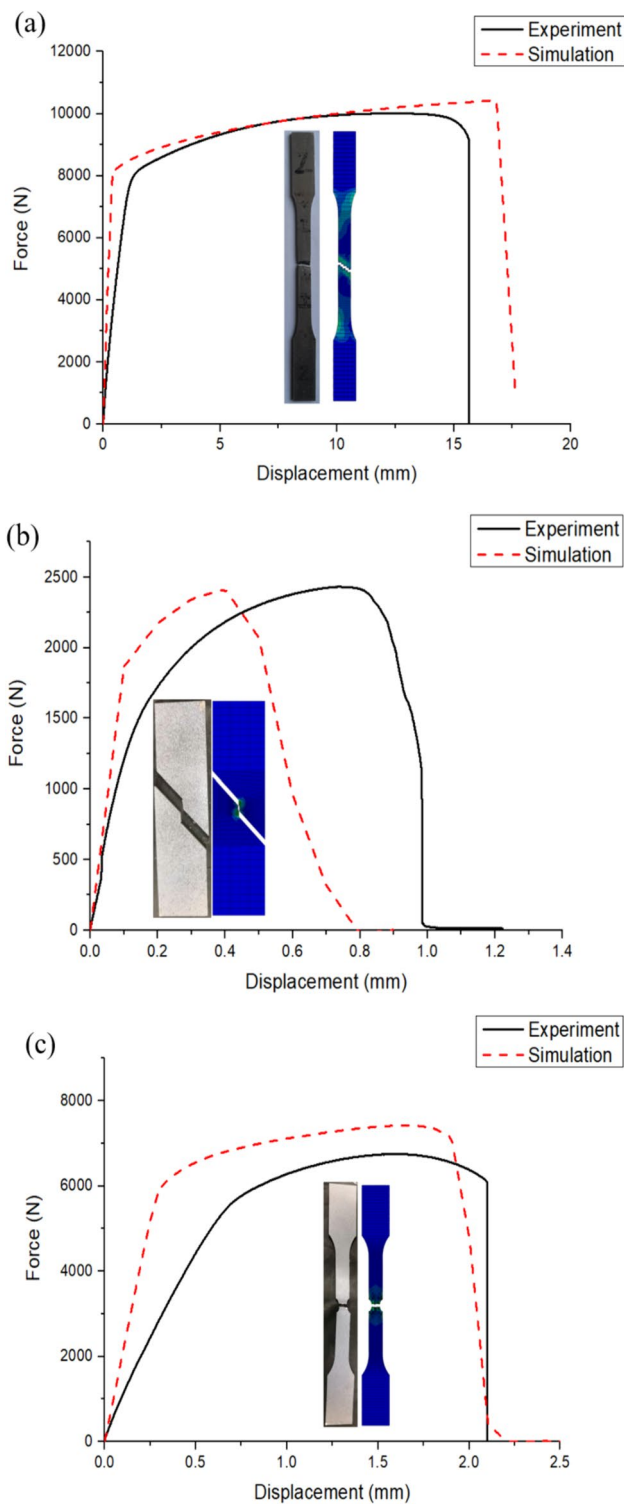


Fig. 12 Comparison of force–displacement curves between experiments and simulations: **(a)** standard tensile specimen, **(b)** shear specimen, and **(c)** notched specimen

failure morphology, the fracture positions of the three specimens obtained from numerical calculations are consistent with the experimental results. The comparison demonstrates

the effectiveness and rationality of Johnson–Cook damage parameters in this research.

Rivet Forming Process

According to the FEM result of the single-lap rivet-bonded hybrid joint, the process of riveting forming has gone through the following: First, when the hybrid joint in Fig. 13(a) was not riveted, there was no stable assembly relationship between the rivet and plates, and there was a clearance-fit between them. Then, the mandrel moved down with the beginning of riveting, and the rivet body with low stiffness was subjected to expansion stress and plastic deformation occurred. As the deformation of the rivet body intensified, the fit relationship between the rivet body and plates gradually transitioned from clearance-fit to interference-fit, as shown in Fig. 13(b). When the main part of the rivet was in close contact with the plate, the surface of the plate formed assembly stress. Finally, when the counterforce of the rivet body against deformation reached the ultimate bearing capacity of the mandrel, which broke at the position of the failure slot, and the riveting process ended. Figure 13(c) showed that there was stress concentration around the riveting holes on the surface of the upper plate. The maximum stress near the riveting holes is about 173 MPa, which does not exceed the yield limit of 6061 aluminium alloy. Figure 13(d) indicated that riveting did not cause damage to the plate. As shown in Fig. 13(e), there was only slight damage at the edge of the adhesive layer hole, indicating that the riveting forming process did not cause large-scale damage to the adhesive layer, thus ensuring the reliability of the manufacturing techniques of the hybrid joint.

Progressive Damage and Failure

The force–displacement curves obtained experimentally and by finite element simulation are presented in Fig. 14(a). It is found that the experimental and numerical curves are in an agreement, and the error between the simulation and the experimental results is within 10%. Figure 14(b) shows the failure morphologies of the hybrid joint in simulation. The rivet hardly shares the shear load in the initial stage, and the crack of the adhesive layer initiates at the end of the aluminium adherend after reaching the peak load. When the energy stored in the adhesive layer reaches the fracture energy of the adhesive layer, the crack propagates rapidly along the plane direction of the adhesive layer. The rivet shares the load as the adhesive layer gradually fails. Since the rivet deviates from the central axis, there is obvious slippage between the plates. Finally, the rivet is individually loaded and has large plastic deformation, which is basically consistent with the experiment.

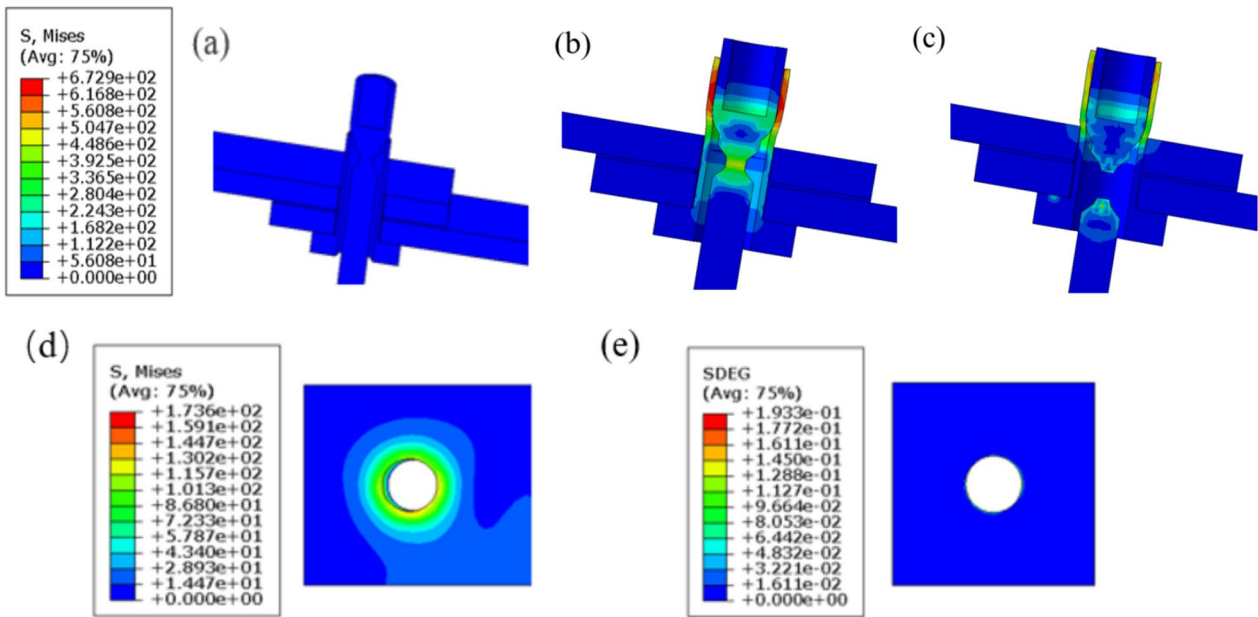
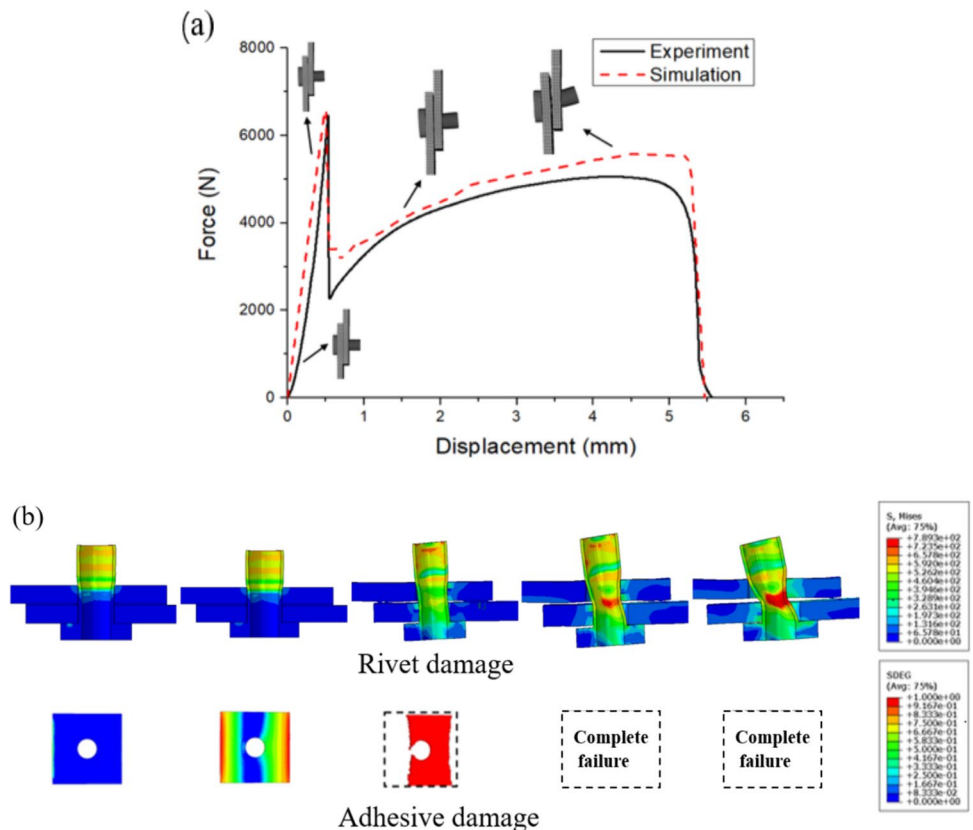


Fig. 13 (a) von Mises stress during rivet forming: initial time, (b) expanded rivet, (c) end of riveting, (d) von Mises stress distribution near the riveting hole of the upper plate, and (e) damage in the adhesive layer

Both experiment and simulation show that the crack of the adhesive layer initiates at the end of the aluminium adherend and gradually extends to the whole adhesive layer. The

rivet deforms under compression and forms a region of high stress on the bearing side in contact with the plate. There is a bending moment in the overlap region of the hybrid joint

Fig. 14 (a) Comparison of force–displacement curves for the single-lap rivet-bonded hybrid joint between experiment and simulation, and (b) damage propagation of the single-lap rivet-bonded hybrid joint in simulation



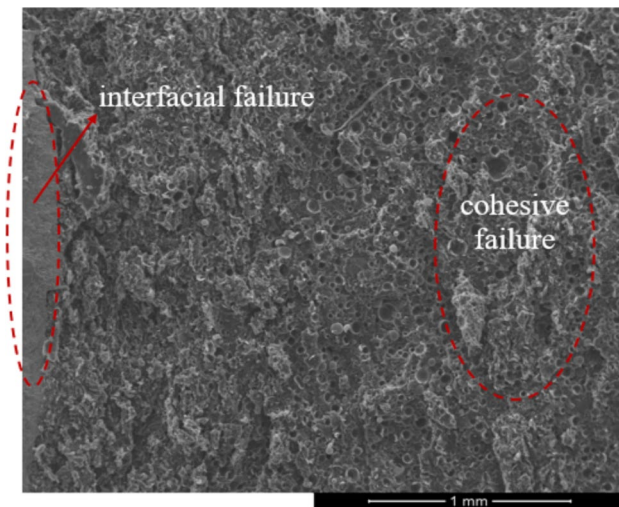


Fig. 15 Scanning electron microscope observation on the failure surface of the adhesive layer

due to the non-collinear load during the quasi-static tension. The peeling force appears at the edge of the overlap region. Therefore, the adhesive layer is not only under shear load, but also under peeling load at the edge of the joint. The adhesive layer has poor stripping resistance, which explains the initial position of adhesive layer failure and the hybrid joint bending phenomenon.

The fracture surface of the adhesive layer is observed through a scanning electron microscope (SEM) as shown in Fig. 15. It can be judged that cohesive failure and interfacial failure are the two main failure modes, where the fracture surface shows homogeneous and consistent waved patterns. Interfacial failure between the substrate and the adhesive layer produces a smoother fracture performance, as seen in the left side of Fig. 15. The presence of a more waved region on the fracture surface suggests that more energy is required for the crack propagation in the adhesive layer. The edge region exhibits features of interfacial failure possibly due to the influence of peeling forces, while the adhesive layer in the centre area displays a uniform hairy appearance indicating cohesive failure.

Conclusions

With the aim of creating a more realistic hybrid joint morphology and preload, this work considered the effect of the riveting forming process and subsequently conducted strength analysis of the single-lap rivet-bonded

hybrid joint. CZM and Johnson–Cook failure criterion were used to numerically simulate the mechanical properties and failure behaviours of the hybrid joint subjected to tensile loading. Three types of specimens were designed to characterize the mechanical properties and Johnson–Cook damage parameters of aluminium and steel. A refined FEM of the hybrid joint was established and damage propagation were investigated. Good agreement was achieved between numerical and experimental results. Major conclusions can be drawn:

The Johnson–Cook damage parameters of 6061 aluminium alloy and 304 stainless steel were calculated, and the reliability of which was verified using experiments and numerical simulations. And a set of experiments and simulation models have been conducted to analyse the deformation and failure of the hybrid joint.

The hybrid joint is reinforced by a preloading due to the riveting forming process. The result of FEM demonstrates that the preloading caused by interference-fit does not introduce damage into the adhesive layer and aluminium adherend during the rivet forming process, which ensures the reliability of the manufacturing techniques of the hybrid joint.

There are two stages in the tensile failure process of the hybrid joint. At the small-displacement stage, the adhesive layer shares most of the applied load, and then brittle fracture occurs until the adhesive layer completely fails. The hybrid joint comes to the large-displacement stage with the complete fracture of the adhesive layer. The rivet bears the load alone and experiences large-scale plastic deformation, which results in the rivet gradually slipping off from the aluminium adherend until the hybrid joint completely fails.

Cracks initiates at the end of the 6061 aluminium adherend and gradually expands to the riveting hole. Multi load transfer path characteristics during the tension of hybrid joint may avoid the instantaneous failure of the rivet-bonded hybrid structure.

Funding The authors would like to acknowledge the financial support from National Natural Science Foundation of China (U21A20165, 52072057 and 12172083), Shanghai Academy of Spaceflight Technology Foundation (SAST2021-060).

Data Availability The data are available from the authors on reasonable request.

Declarations

Conflict of Interests The authors declared no potential conflicts of interest with respect to the research, authorship, and/or publication of this article.

References

- Chen Y, Li M, Yang X, Luo W (2020) Damage and failure characteristics of CFRP/aluminium single lap joints designed for lightweight applications. *Thin-Walled Struct* 153:106802
- Jeevi G, Nayak SK, Abdul Kader M (2019) Review on adhesive joints and their application in hybrid composite structures. *J Adhes Sci Technol* 33(14):1497–1520
- Nemati Giv A, Ayatollahi MR, Ghaffari SH, da Silva LF (2018) Effect of reinforcements at different scales on mechanical properties of epoxy adhesives and adhesive joints: a review. *J Adhes* 94(13):1082–1121
- Semoto T, Tsuji Y, Yoshizawa K (2012) Molecular understanding of the adhesive force between a metal oxide surface and an epoxy resin: Effects of surface water. *Bull Chem Soc Jpn* 85(6):672–678
- Dawei Z, Qi Z, Xiaoguang F, Shengdun Z (2018) Review on joining process of carbon fiber-reinforced polymer and metal: methods and joining process. *Rare Metal Mater Eng* 47(12):3686–3696
- Maggiore S, Banea MD, Stagnaro P, Luciano G (2021) A review of structural adhesive joints in hybrid joining processes. *Polymers* 13(22):3961
- Marques EAS, Da Silva LF, Banea MD, Carbas RJC (2015) Adhesive joints for low-and high-temperature use: an overview. *J Adhes* 91(7):556–585
- Viana GMSO, Costa M, Banea MD, Da Silva LFM (2017) A review on the temperature and moisture degradation of adhesive joints. *Proc Inst Mech Eng Pt L J Mater Des Appl* 231(5):488–501
- Sadowski T, Golewski P, Zarzeka-Raczowska E (2011) Damage and failure processes of hybrid joints: adhesive bonded aluminium plates reinforced by rivets. *Comput Mater Sci* 50(4):1256–1262
- SJ A, Natarajan A (2022) Review on the advancements and relevance of emerging joining techniques for aluminium to polymers/carbon fibre-reinforced polymer lightweight hybrid structures. *Proc Inst Mech Eng Pt L J Mater Des Appl* 236(12):2394–2435
- El Zaroug M, Kadioglu FERHAT, Demiral M, Saad D (2018) Experimental and numerical investigation into strength of bolted, bonded and hybrid single lap joints: Effects of adherend material type and thickness. *Int J Adhes Adhes* 87:130–141
- Sadowski T, Zarzeka-Raczowska E (2012) Hybrid adhesive bonded and riveted joints-influence of rivet geometrical layout on strength of joints. *Arch Metall Mater* 57:1128–1135
- Kang TY, Aan HS, Chun HJ, Park JC (2023) Fatigue and tensile behaviours of high stiffness adhesive bonded and hybrid joints with composite-steel dissimilar materials. *Int J Precis Eng Manuf* 24(4):645–656
- Sousa FC, Zamani P, Akhavan-Safar A, da Silva LFM (2023) A comprehensive review of the SN fatigue behaviour of adhesive joints. *J Adv Join Proc* 9:100178
- Hao Z, Chen G, Ke H, Deng L, Liu L (2022) Characterization of out-of-plane tensile stress-strain behaviour for GFRP composite materials at elevated temperatures. *Compos Struct* 290:115477
- Zhang H, Zhang L, Liu Z, Zhu P (2021) Research in failure behaviours of hybrid single lap aluminium-CFRP (plain woven) joints. *Thin-Walled Struct* 161:107488
- Kelly G (2005) Load transfer in hybrid (bonded/bolted) composite single-lap joints. *Compos Struct* 69(1):35–43
- Chowdhury NM, Chiu WK, Wang J et al (2016) Experimental and finite element studies of bolted, bonded and hybrid step lap joints of thick carbon fibre/epoxy panels used in aircraft structures. *Compos Pt B-Eng* 100:68–77. <https://doi.org/10.1016/j.compositesb.2016.06.061>
- Bodjona K, Lessard L (2015) Load sharing in single-lap bonded/bolted composite joints. Part II: Global sensitivity analysis. *Compos Struct* 129:276–283
- Raju KP, Bodjona K, Lim GH, Lessard L (2016) Improving load sharing in hybrid bonded/bolted composite joints using an interference-fit bolt. *Compos Struct* 149:329–338
- Esmaili-Goldarag F, Babaei A, Jafarzadeh H (2018) An experimental and numerical investigation of clamping force variation in simple bolted and hybrid (bolted-bonded) double lap joints due to applied longitudinal loads. *Eng Fail Anal* 91:327–340
- Lopez-Cruz P, Laliberté J, Lessard L (2017) Investigation of bolted/bonded composite joint behaviour using design of experiments. *Compos Struct* 170:192–201
- Hai ND, Mutsuyoshi H (2012) Structural behaviour of double-lap joints of steel splice plates bolted/bonded to pultruded hybrid CFRP/GFRP laminates. *Constr Build Mater* 30:347–359
- Xiaoqi LI, Cheng X, Cheng Y, Zhiyong WA, Huang W (2021) Tensile properties of a composite-metal single-lap hybrid bonded/bolted joint. *Chin J Aeronaut* 34(2):629–640
- Golewski P, Sadowski T (2019) The influence of single lap geometry in adhesive and hybrid joints on their load carrying capacity. *Materials* 12(12):1884
- ASTM D5868-01 (2014) Standard test method for lap shear adhesion for fiber reinforced plastic (FRP) bonding. American Society for Testing and Materials, West Conshohocken, PA, USA
- Zheng G, Wang H, Han X, Li W (2021) Mechanical behavior of AL/CFRP single-lap joint subjected to combined thermal and constant loading. *J Adhes* 97(4):361–379
- Han X, Jin Y, da Silva LF, Costa M, Wu C (2019) On the effect of adhesive thickness on mode I fracture energy-an experimental and modelling study using a trapezoidal cohesive zone model. *J Adhes* 96:490–514
- Budhe S, Banea MD, de Barros S, Da Silva LFM (2017) An updated review of adhesively bonded joints in composite materials. *Int J Adhes Adhes* 72:30–42
- Islam MS, Tong L, Falzon PJ (2014) Influence of metal surface preparation on its surface profile, contact angle, surface energy and adhesion with glass fibre prepreg. *Int J Adhes Adhes* 51:32–41
- Naito K, Onta M, Kogo Y (2012) The effect of adhesive thickness on tensile and shear strength of polyimide adhesive. *Int J Adhes Adhes* 36:77–85
- Kanerva M, Saarela O (2013) The peel ply surface treatment for adhesive bonding of composites: A review. *Int J Adhes Adhes* 43:60–69
- Siegel A, Laporte S, Sauter-Starace F (2021) Johnson-Cook parameter identification for commercially pure titanium at room temperature under quasi-static strain rates. *Materials* 14(14):3887
- Hong T, Ding F, Chen F, Zhang H, Zeng Q, Wang J (2023) Study on the fracture behaviour of 6061 aluminium alloy extruded tube during different stress conditions. *Crystals* 13(3):489
- De Sousa CCRG, Campilho RDSG, Marques EAS, Costa M, da Silva LF (2017) Overview of different strength prediction techniques for single-lap bonded joints. *Proc Inst Mech Eng Pt L J Mater Des Appl* 231(1–2):210–223
- Da Costa RR, De Medeiros R, Ribeiro ML, Tita V (2017) Experimental and numerical analysis of single lap bonded joints: Epoxy and castor oil PU-glass fibre composites. *J Adhes* 93(1–2):77–94
- Sadeghi A, Mahshid R, Heidari-Rarani M, Lessard L (2022) Effect of lamina fibre orientation interfaced with semi-flexible

- adhesive layer on strength and failure mode of composite single-lap joints. *Int J Adhes Adhes* 118:103232
38. Fernandes FJ, Pavanello R (2022) Topology optimization of adhesive material in a single lap joint using an evolutionary structural optimization method and a cohesive zone model as failure criterion. *Proc Inst Mech Eng Pt L J Mater Des Appl* 236(4):757–778
 39. Constante CJ, Campilho RDSG, Moura DC (2015) Tensile fracture characterization of adhesive joints by standard and optical techniques. *Eng Fract Mech* 136:292–304
 40. Sadeghi MZ, Zimmermann J, Saravana K, Gabener A, Dafnis A, Schröder KU (2020) Influence of fracture envelope on FE failure

load prediction of adhesively bonded joints by using mixed mode bending tests. *Procedia Struct Integr* 28:1601–1620

Publisher's Note Springer Nature remains neutral with regard to jurisdictional claims in published maps and institutional affiliations.

Springer Nature or its licensor (e.g. a society or other partner) holds exclusive rights to this article under a publishing agreement with the author(s) or other rightsholder(s); author self-archiving of the accepted manuscript version of this article is solely governed by the terms of such publishing agreement and applicable law.